WILLIAM J. TROPF, MICHAEL E. THOMAS, TERRY J. HARRIS, and STEVEN A. LUTZ

PERFORMANCE OF OPTICAL SENSORS IN HYPERSONIC FLIGHT

Hypersonic flight through the atmosphere presents unique environmental conditions that significantly affect the performance of a vehicular optical sensor. Knowledge of high-speed optical conditions and of the resulting effects on sensor performance is important in the design of optical instruments used in space shuttles, high-speed aircraft, and guided missiles. This article reports on recent work to quantify the transmissive and radiative effects of complex flow and heated windows caused by hypersonic flight in order to predict sensor performance and investigate the effect of film cooling of windows.

INTRODUCTION

Basic flow features that affect optical performance in supersonic flight are illustrated in Fig. 1. The outermost effect is the sharp density gradient at the shock wave in front of the optical window. The density gradient refracts optical rays and acts as a lens. Shocks from other parts of the forward vehicle body will also refract optical rays and may interact with the window shock to form a complex optical path. Gas behind the shock is highly compressed and heated. Density variations in this compressed flow create refractive index variations and act as a gradient-index lens.

A second effect of compressed flow is aerodynamic heating of the window itself. The window temperature greatly affects the density in the boundary layer. If the window temperature or stress-causing thermal gradients (thermal shock) become excessively high, a film-cooling gas can be injected directly into the boundary layer to give thermal protection. Such cooling further complicates flow and heat-transfer conditions. The principal optical effects are resolution (blur and defocus), boresight error, and radiation from gases and windows, which can significantly alter sensor performance.

High resolution is desirable for detection (including clutter rejection), tracking accuracy, and recognition. Generally, the detector size is matched to the optical resolution; therefore, a loss of resolution because of blurring or defocusing results in decreased signal and reduced angular accuracy. Conversely, an oversized detector reduces capabilities in recognition, angle measurement, and clutter rejection, and increases noise. Therefore, a knowledge of the optical effects of hypersonic flight will avoid sensor performance degradation.

Boresight error can affect performance in several ways. Boresight fluctuations (caused by turbulence, shock interaction, or coolant mixing) can blur images, cause errors in data transmission, and induce angle noise in trackers. Changes in boresight caused by body motion (e.g., changing shock structure or window distortion) appear as position errors or tracking rate errors that adversely affect sensors used for guidance and navigation.

Radiation from the compressed gases and aerodynamically heated window heats interior components and can increase sensor noise. Heating of interior components leads to re-radiation and increased background noise. Temperature-sensitive components suffer degradation as a result of overheating, thermal expansion, increased friction, or changes in operation. Highly sensitive infrared photodiodes, whose noise performance is limited by the

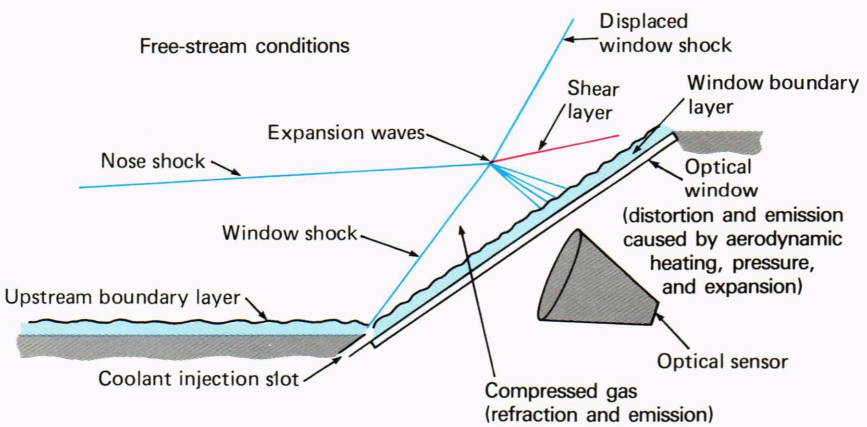

Figure 1—Hypersonic flow around an optical window. High-speed flight produces a complex optical environment, including refraction and radiation from the gases and the aerodynamically heated window.

background radiation, will experience increased noise. Multiplexed photodiodes, whose dynamic ranges are limited by the multiplex process, can be saturated when the background radiation is high enough, precluding measurements of any kind.

An integrated, interdisciplinary approach (including fluid dynamics, heat transfer, optics, and material science input) is necessary to understand, model, and measure the effect of high-speed flight on optical sensors. This article discusses optical effects of hypersonic flight and reports on analytical and experimental advances (funded as APL Independent Research and Development) that quantify these effects and their impact on sensor performance. The work performed includes prediction and measurement of the refractive effects of hypersonic flow, analysis of film cooling (and experiments that are planned), absorption and index measurements of gases, and both theoretical and experimental optical characterization of materials at high temperatures.

FLOW AROUND OPTICAL WINDOWS IN HYPERSONIC FLIGHT

Aerodynamic bodies flying through the atmosphere compress air at the leading edges, resulting in pressures and temperatures that are higher than ambient conditions. At supersonic speeds, the disturbed air lies behind a shock or density discontinuity. As speed increases, the strength of the shock (i.e., the pressure rise across the shock) and the temperature behind the shock increase rapidly. Increasing speed also causes the shocks to bend more sharply and lie closer to the body. By the time hypersonic speed (speeds greater than Mach 5) is obtained, air temperature behind the shock is very high, and surfaces (e.g., optical windows) experience high heating rates caused by viscous friction in the flow boundary layer.

High-temperature gases surrounding the sensor may radiate significantly and are high in density; hence they have increased refractive power. For air, the refractive index (n) is defined by the Gladstone–Dale relationship (a simplification of the Lorentz–Lorenz equation) given by (see the table of symbols)

$$n - 1 = \beta\rho \ , \qquad (1)$$

where β is a wavelength-dependent constant and ρ is the mass density of the air. Reference 1 gives the values of β for wavelengths from 0.2 to 10 μm; for wavelengths longer than 1 μm, β has a nearly constant value of 2.2×10^{-4} m^3/kg. Under some conditions, the simple Gladstone–Dale formula is insufficient, and higher order terms must be considered. This case will be discussed further in the section on coolant gas properties.

Hypersonic flow is conveniently characterized in terms of density ratios referenced to free-stream (unperturbed air) conditions. Referring to Fig. 1, there are density changes associated with shock waves, expansion waves, shear layers produced by shock interactions, and the boundary layer surrounding the body. Shock and expansion waves are adequately described using supersonic inviscid flow theory, in which viscosity, thermal conduction, and mass diffusion are neglected. Boundary layer theory augments inviscid results to describe the behavior of flow in shear and surface boundary layers. Density profiles associated with the flow field effects identified in Fig. 1 are discussed further below.

Symbols

α	=	absorption coefficient
β	=	constant in Gladstone–Dale relationship
δ	=	boundary layer thickness; vibrational mode width
ϵ	=	emissivity; dielectric constant
θ	=	shock angle
μ	=	absolute viscosity
ν	=	wave number
ρ	=	density
τ	=	transmittance
ω	=	frequency, in rad/s
Σ	=	summation over index n
A	=	linear coefficient of gas index with P/RT
B	=	quadratic coefficient of gas index with P/RT
C_p	=	heat capacity (constant pressure)
d	=	shock standoff distance
E	=	coolant effectiveness
E_ν	=	spectral radiance
H	=	enthalpy
R	=	gas constant
M	=	Mach number
m	=	coolant-to-edge mass flux ratio
$\dot{m}$	=	mass flow rate (of coolant) per unit width
n	=	index of refraction (real part)
P	=	pressure
Re	=	Reynolds number
R	=	radius (of blunt nose)
r	=	single-surface reflectivity
T	=	temperature (absolute); T^* is reduced temperature (dimensionless)
t	=	thickness
s	=	(coolant) slot height
u	=	(coolant) velocity
x	=	distance along flow direction
y	=	distance normal to flow

Subscripts

aw	=	adiabatic wall
bl	=	boundary layer
c	=	coolant
e	=	edge (of boundary layer) conditions
en	=	entrained quantity from edge of boundary layer
∞	=	free-stream conditions; high frequency
n	=	index for summation
o	=	stagnation conditions; fundamental frequency
p	=	constant pressure
s	=	slot
x	=	length
2	=	condition behind shock
λ	=	function of wavelength

Shock and Expansion Waves

A shock is a discontinuity in a supersonic flow. Fluid (air) crossing a stationary shock rises abruptly in pressure and decreases in velocity. In air, the density downstream from the shock, ρ_2, referenced to the free-stream density, ρ_∞, and Mach number, M_∞, is expressed as

$$\frac{\rho_2}{\rho_\infty} = \frac{6(M_\infty \sin\theta)^2}{(M_\infty \sin\theta)^2 + 5}, \qquad (2)$$

an expression derived from oblique shock theory. For sharp cones, in the hypersonic limit ($M \to \infty$), the shock angle, θ, is about 13/12 the cone semivertex angle. For cones with a semivertex angle greater than about 57°, the shock detaches from the cone tip and a blunt-body shock is formed. The shock angle directly in front of a blunt body is nearly 90° and the flow is approximately normal to the shock. For normal shock flow approaching the hypersonic limit, the density ratio of Eq. 2 approaches a maximum value of 6.

In contrast to the abrupt changes in flow associated with shock waves, flow properties undergo continuous change across an expansion wave. These waves are caused by shock–shock interactions and convex corners along surfaces. Density, pressure, and temperature ratios decrease through the expansion wave while the Mach number increases. In Fig. 1, the expansion wave emanating from the shock–shock interaction serves as a mechanism for turning the supersonic flow direction to satisfy continuity requirements. The expansion wave flow field must be determined iteratively by adjusting the displacement shock and expansion wave to find the condition of equal pressure and flow angles on either side of the shear layer that satisfies continuity requirements.

Boundary Layer Flow

Flow behavior in shear and surface boundary layers can be described using boundary layer flow equations. Boundary layer theory differs from shock and expansion wave theory in that viscosity, thermal conductivity, and mass diffusion effects dominate flow behavior. A common assumption used for surface (wall) boundary layers is constant pressure across the layer. Combining the gas equation of state (e.g., ideal gas law) and the constant-pressure assumption allows determination of the density profile from the temperature solution. Density profiles of a fully developed, turbulent, compressible, Mach 5 boundary layer over a flat plate are shown in Fig. 2. These profiles are determined from the Crocco–Busemann temperature solution[2] for two limiting conditions: (1) adiabatic wall (no heat transfer to the wall) and (2) cold wall (maximum heat transfer) conditions. The cold-wall density approaches infinity at the wall, creating a sharp density gradient. The adiabatic-wall density ratio (referenced to the density at the edge of the boundary layer) has a value of 0.182 at the wall.

Shear layers are also characterized by boundary layer theory. The same basic equations for wall boundary layers apply. Boundary conditions and the shear layer mixing model are different. Density across a shear layer depends on the density and velocity differences of the flow on either side.

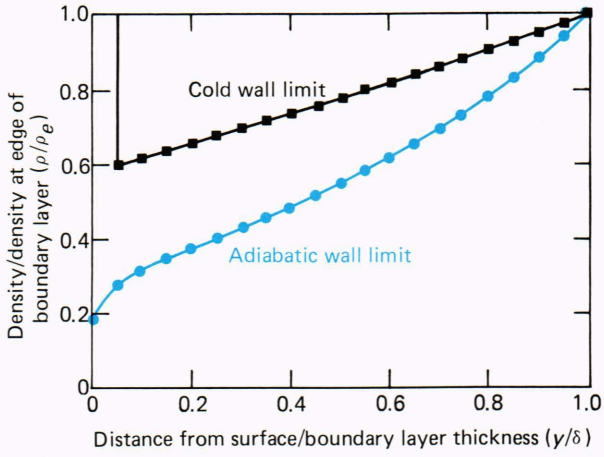

Figure 2—Density profiles in a Mach 5 turbulent boundary layer. The boundary layer density, ρ, is normalized by the density at the edge of the layer; distance through the layer, y, is normalized by the boundary layer thickness, δ.

Blunt-Body Shock Structure

A hypersonic window, particularly one mounted in the nose of a vehicle, may be in the form of a blunt body. A typical blunt-body flow field is shown in Fig. 3. The shock wave is detached and normal shock relations are used to estimate the change in density along the stagnation streamline. A complete flow-field and shock-structure solution depends on body geometry and flight Mach number. Such solutions are complex because of the mixed subsonic ($M < 1$) and supersonic ($M > 1$) regions in the flow field. The governing equations are mathematically elliptical in the subsonic region and hyperbolic in the supersonic region. Time-dependent numerical techniques are used to determine flow fields surrounding blunt bodies. Inviscid flow results of Fig. 3 were calculated using MacCormack's predictor–corrector algorithm. The density gradient from shock to blunt-body surface depends on the density change behind the shock and the shock standoff distance. An empirical formula for the shock standoff distance, d_0, at the tip of a conical body with a spherical nose is

$$d_0/R = 0.143\, e^{[3.24/M_\infty^2]}, \qquad (3)$$

where R is the nose radius.[3] This equation shows the shock standoff distance decreasing with Mach number.

Figure 4 shows a typical blunt-body refractive index result along the stagnation streamline of a hemispherical blunt body (see Fig. 3). Density results, calculated from thin-layer Navier–Stokes equations, are combined with the Gladstone–Dale Law to determine the index of refraction for two cases: cold wall and hot wall (after 15 s of aerodynamic heating). These results are typical of those used in the optical analysis described below.

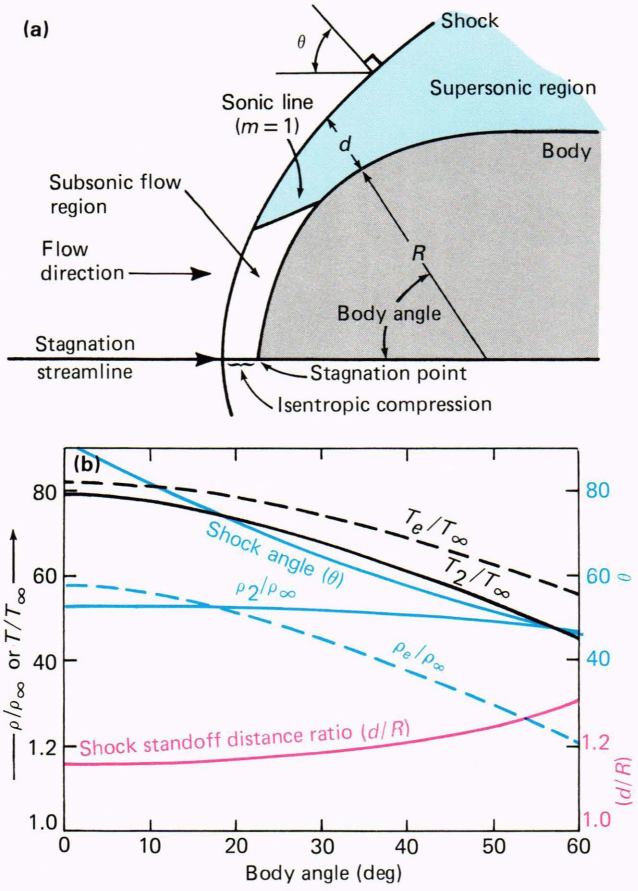

Figure 3—The flow field surrounding a hemispherical blunt body at Mach 6. (a) shows the subsonic and supersonic regions behind the shock and identifies the stagnation streamline. (b) gives inviscid flow temperature and density (references to free-stream conditions), shock angle, and shock distance from the body (references to body radius).

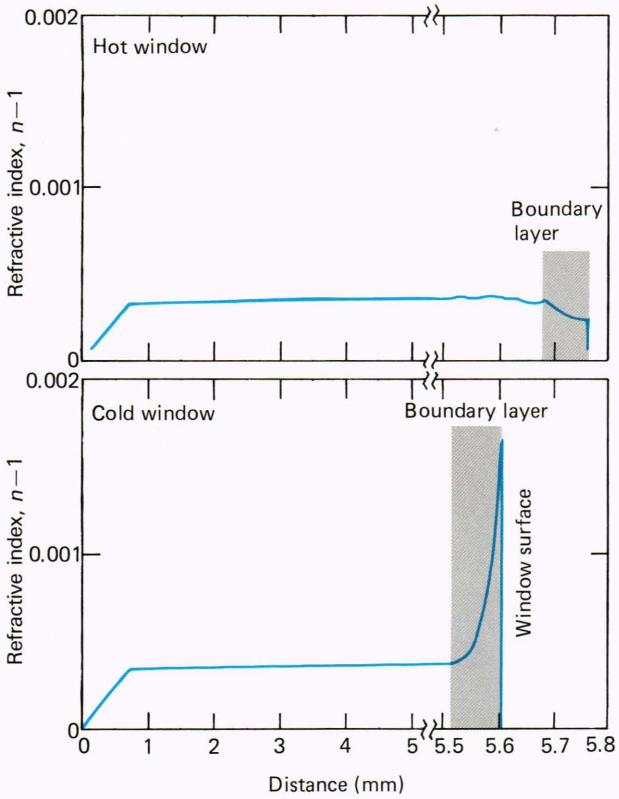

Figure 4—The refractive index along the stagnation streamline of a 7.1-cm-diameter hemisphere at Mach 6. Note the scale change that exaggerates the depth of the boundary layer. Optical effects of the boundary layer are small because of its small size.

Shock Wave Impingement on Blunt-Body Flows

The impingement of a forward shock (from the nose of a vehicle) on a blunt-body shock wave can create several possible interference flow fields. These interference patterns are characterized by Edney.[4] The most severe heating condition results when the shock interaction occurs in front of the subsonic region (see Fig. 3). If the impinging shock strength and free-stream Mach number are sufficiently high, an embedded supersonic jet (toward the surface) can be created. The jet region, bounded by shear layers, has a reported width of 3° of body surface arc.[4-6] Peak heating values of approximately 16 and 10 times the undisturbed stagnation point value for a spherical body[5] and for a cylinder,[6] respectively, have been reported. This intense heating will create severe local thermal gradients that cause optical degradation because of thermal expansion and refractive index change. If heating rates become excessive, active cooling may be necessary to ensure survival or to maintain the window at acceptable temperatures.

APL has a test facility capable of simulating the flow conditions (speed, temperature, and pressure) and heat transfer of hypersonic flight. The facility, part of the Propulsion Research Laboratory, is being instrumented to give a unique optical testing capability in high-speed flow.[7] One capability of the facility is the production of shock interference using a movable shock-generating probe. The test setup is shown in Fig. 5a. The hypersonic free jet emerges from the nozzle and surrounds the test article mounted on a sting. A movable shock generator is lowered into the hypersonic flow from the top of the test cabin. The shock generator consists of a rod with a wedge-shaped end. When the end is lowered into the flow, a second shock is created ahead of the test article. As the wedge is lowered, this second shock interacts with the blunt-body shock surrounding the test article. Shadowgraphs are used to observe the shock structure. Figures 5b, 5c, and 5d show the shock interaction with a hemispherical window. Figure 5b shows the blunt-body shock alone, Fig. 5c shows one type of shock interaction that creates a shear layer across the test article body, and Fig. 5d shows the interaction that occurs when a supersonic jet impinges on the test article surface. The last two cases create severe refractive disturbances and very high aerodynamic heating. The sapphire dome shown here survived this transient shock impingement condition. Optical measurements made with the setup are discussed below.

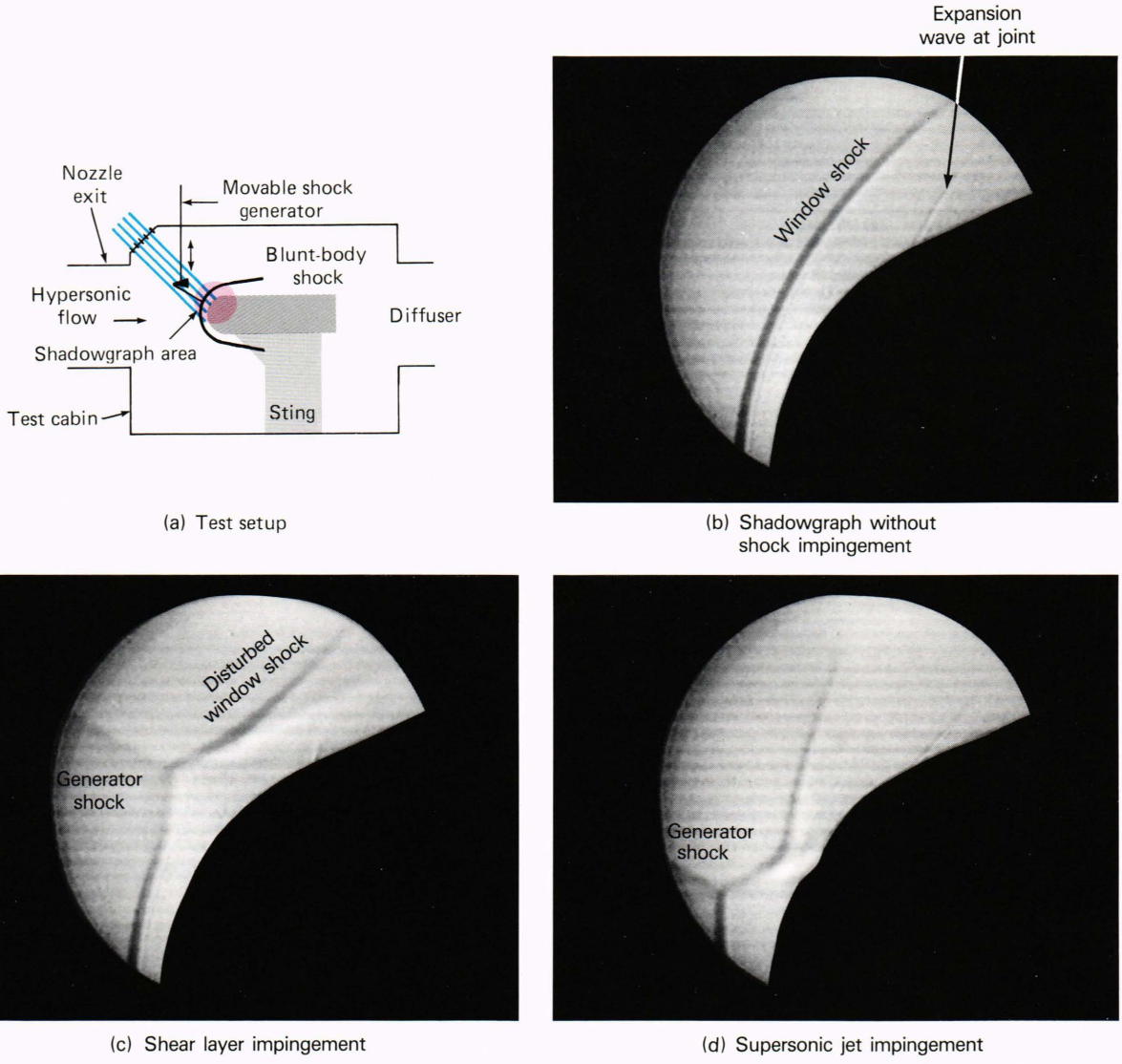

Figure 5—Shadowgraphs of shock wave impingement on a sapphire hemispherical window at Mach 5. (a) A sketch of the shock generator and resulting shadowgraphs of (b) the blunt-body shock alone, (c) shock interaction with shear layer impingement, and (d) shock interaction with supersonic jet impingement.

Air Temperature, Flow-Field Radiation, and Aerodynamic Heating

Air compressed in front of a body in hypersonic flight experiences a sharp rise in temperature. For example, the static temperature increase behind a normal shock (T_2) in air is

$$T_2/T_\infty = (7\,M_\infty^2 - 1)\,(M_\infty^2 + 5)/36\,M_\infty^2 \quad . (4)$$

The temperature T_2 approximates the static temperature behind the normal portion of a blunt body shock. Although the thickness of the compressed layer is small (0.157 times the radius of a hemispherical nose at Mach 6; Eq. 3), temperature and pressure are high enough to produce significant radiation.

The principal radiation in the compressed gas comes from carbon dioxide and water, which are the primary infrared-active gases of the atmosphere. Figure 6 shows the calculated spectral radiance from the stagnation region of a hemisphere in Mach 6 flight at an altitude of 24.4 km. Significant radiation (an order of magnitude greater than earth scene thermal emission) emanates from the 2300 cm^{-1} band of carbon dioxide and the 3700 cm^{-1} band of water, despite the very low emissivity of this short segment of gas. Note that the radiation in these two bands exceeds that of a nominal 300 K scene background. Much greater radiation will result from lower altitude flight because of increased ambient pressure and, at very low altitudes, significantly higher water vapor concentration. Gases injected into the boundary layer as a film coolant (see below) may also be a source of significant infrared radiation.

The blunt-body aerodynamic heating rate is proportional to the velocity gradient at the edge of the boundary layer and the enthalpy difference between the stagna-

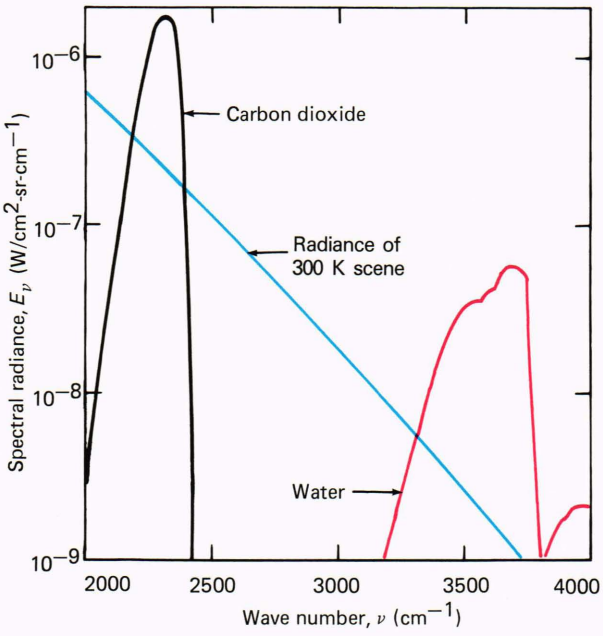

Figure 6—Radiance of gases along the stagnation streamline of a 7.1-cm-diameter hemisphere at Mach 6 flight at an altitude of 24.4 km. Calculated radiance (brightness) of high-temperature gases behind the normal shock of a hemisphere exceeds that of a nominal 300 K background.

tion and wall conditions. The enthalpy, H, and temperature are related by

$$dH = C_p \, dT \, , \tag{5}$$

where C_p is the specific heat at constant pressure. Stagnation temperature is given by

$$T_0 / T_\infty = 1 + 0.2 \, M_\infty^2 \, . \tag{6}$$

Stagnation heating is highest when the wall is cold and decreases as the wall temperature asymptotically approaches equilibrium temperature. As a window heats, it becomes an additional radiation source that can exceed that of the background scene or the compressed gas behind the shock.

AERO-OPTICAL EFFECTS OF HYPERSONIC FLOW

The aero-optical effects of hypersonic flow are determined by using the results of flow density calculations as the input to optical ray-trace codes that determine blurring and boresight error. This work has concentrated on calculating and understanding the optical effects of simpler flight conditions in order to gain an appreciation of the magnitude of the optical effects, to develop computational techniques, and to guide development and evaluation of equipment that will be used to measure optical effects under simulated high-speed flight conditions. Optical effects of complicated flow structures and highly transient events (such as shock-wave impingement on a side-mounted sensor) are best determined experimentally.

Aero-Optical Computations

Initial work has focused on hemispherical windows (domes) that give good optical performance over a large optical field of view. Such windows are commonly used for missile optical guidance systems, and they have the advantage of an axisymmetric flow field for ease of fluid dynamic and optical calculation.

Density results from fluid flow calculations are converted to the refractive index using Eq. 1, the Gladstone–Dale relationship (a typical example is shown in Fig. 4). Table 1 lists the flight conditions used in this optical performance study. The variable index of refraction of air in front of the dome is then modeled as a series of thin lens elements, each with a power-series description of the two-dimensional (radial and axial) gradient index, for exact ray tracing. In addition to flow-field effects, optical effects of the deformation of the window caused by aerodynamic heating were evaluated using a heat transfer code to determine window temperature and a finite-element stress code to determine the window shape after heating.

Optical calculations are compared with the diffraction-limited performance of a sensor operating at 4 μm. Using a 3.0-cm-diameter optical system behind a 3.5-cm radius, 0.25-cm-thick dome, the most significant effect is a slight focus shift that increases geometric blur to a level still smaller than a 4-μm-wavelength diffraction-limited spot size (as represented by the Airy radius). Figure 7 shows typical results. The blur caused by focus shift can be easily removed by refocusing to obtain optimum performance. Wavefront maps show no more than a one-quarter wavelength distortion (at 4-μm wavelength) across the exit pupil. Boresight shifts are very small, the largest being about 0.01 mrad.

Results from optical resolution studies of the flow over hemispherical windows (including shock wave, compressed flow behind the shock, and the boundary layer) show very small changes in resolution and boresight for an infrared system operating at 4 μm. Since the reference Airy radius is proportional to wavelength over the aperture diameter, ultimate angular resolution of a visible wavelength sensor (of the same aperture) is much smaller than that of an infrared system, and flow-induced blurring will dominate resolution.

Table 1—Flight conditions used for aero-optical computations.

	Flight Condition		
Case	*Speed (Mach)*	*Altitude (km)*	*Window Attachment*
1	4.0	0.3	None (free expansion)
2	5.0	15.2	None (free expansion)
3	6.5	30.5	None (free expansion)
4	5.0	15.2	Rigid (constrained expansion)
5	5.0	15.2	Titanium ring (partially constrained expansion)

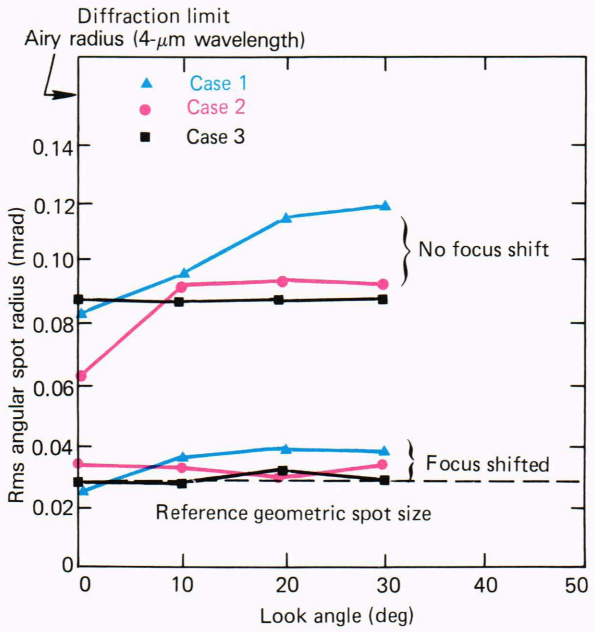

Figure 7—Resolution of a small optical system in several flight conditions. The shock, compressed gases, and boundary layer surrounding a cold hemispherical window in high-speed flight cause some blurring that can be corrected by a focus shift. In the infrared, the focus change is smaller than the diffraction-limited spot size (Airy radius).

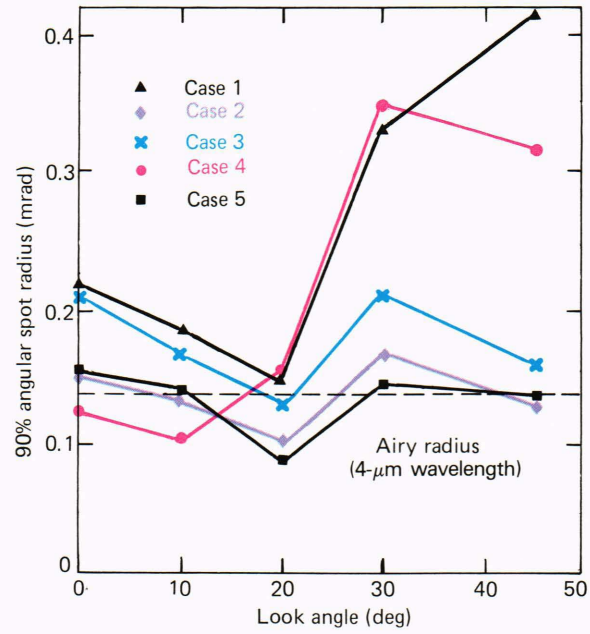

Figure 8—Resolution of a small optical system after aerodynamic heating of the window. The nonuniform aerodynamic heating of a hemispherical window after 15 s exposure to several flight conditions shows a significant thermal distortion of the window. In the infrared, this distortion is up to twice the diffraction limit.

Thermal expansion of a hemispherical window has a significantly larger effect on optical performance. Aerodynamic heating produces a significant temperature gradient around the window that translates into a distortion in shape through thermal expansion. Figure 8 shows the resulting resolution as a function of look angle (i.e., the angle from the stagnation line) for several conditions after 15 s of heating.

Further examination of optical performance shows significant deviation of optical rays across the aperture and shows that the deviation increases as the size of the aperture increases. This effect is shown in Fig. 9, where larger apertures are presented as pupil coordinates greater than unity. A typical wavefront map (Fig. 10) shows much larger thermal expansion distortion (at 4 μm) across the pupil compared with that caused by hypersonic flow alone. Boresight errors caused by dome distortion are also larger, with a peak value as high as 0.5 mrad.

Combined effects of the flow-field and dome thermal expansion distortions show that, as expected, expansion dominates and determines both resolution and boresight error.

Vehicle nose-shock refraction on a side-mounted optical system was evaluated as an independent effect. (Note that the flow field surrounding a vehicle will affect the flow surrounding an optical window, hence the effects are not completely independent.) A conical shock is assumed (Eq. 2), although this representation is strictly true only for conical forebodies with no angle of attack. A 15° forebody half-angle is used to determine shock parameters.

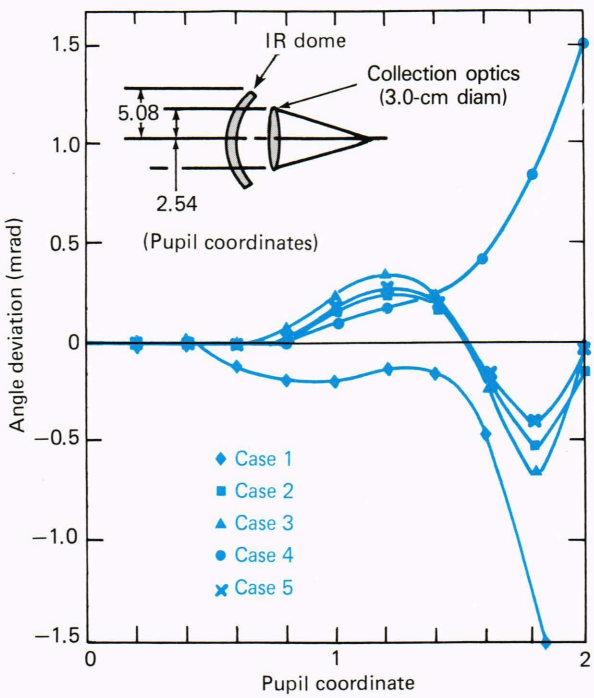

Figure 9—Optical ray deviation in heated windows as a function of pupil coordinate. The deviation of individual rays shows that the on-axis blurring is principally caused by marginal rays. If the collecting aperture is increased, blurring will be much greater.

The conical shock surface introduces a significant amount of asymmetry to the calculation of optical per-

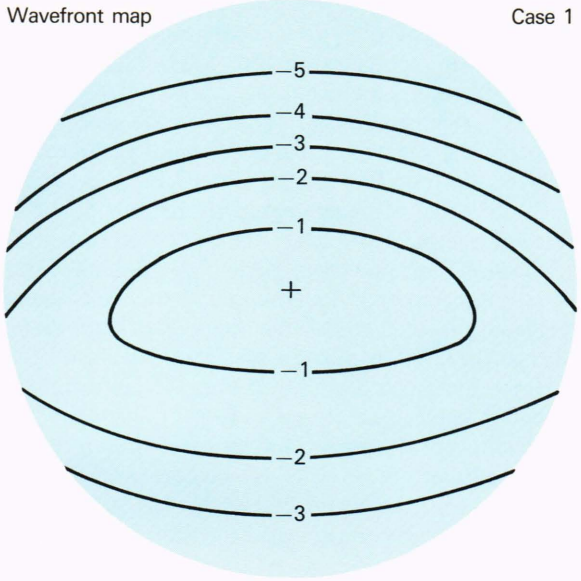

Figure 10—Wavefront map showing the distortion of a heated window. The optical path difference across the pupil, in one-quarter wavelengths at 4 μm, is shown for a hemispherical window exposed for 15 s at Mach-4, 30-m-altitude flight conditions and a 45° look angle. A similar map for a cold dome shows a maximum one-quarter-wavelength optical path difference.

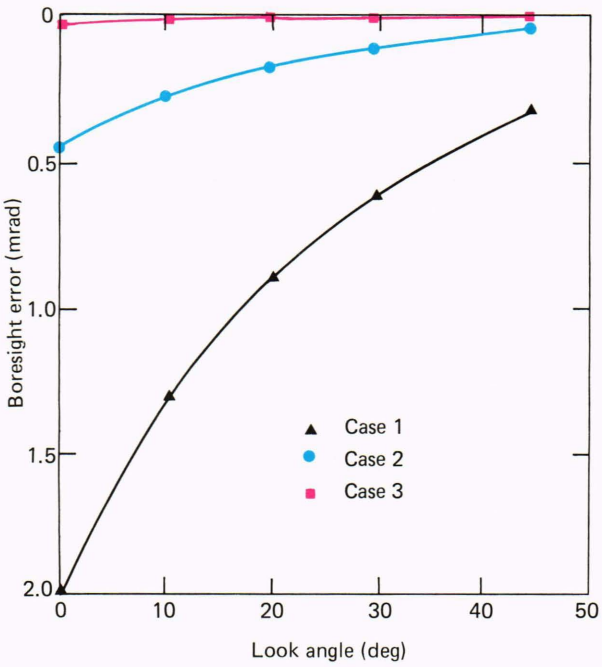

Figure 11—Boresight error from a conical nose shock off a 15° (half-angle) forebody. The bow shock in front of a side-mounted optical sensor can experience a significant boresight error.

formance. In one plane, the conical shock has no curvature (hence, no focusing power); in the other plane, it has curvature that varies along the shock. The difference in the two planes will cause astigmatism in the image, although for the flight conditions examined, the astigmatic asymmetry is quite small. A more significant nose-shock effect is boresight error, which can be as high as 2 mrad when looking directly forward (Fig. 11).

An angle of attack in the plane of a side-mounted window will cause significant changes to the optical effects. On the windward side, there will be a significant increase in air density and heat transfer, and, if the angle of attack is significantly great, impingement of the nose shock on the sensor window. On the leeward side, the boundary layer of the vehicle body enlarges and can begin to cover the seeker aperture. Figure 12 schematically shows these effects in the form of crossflow density contours at a typical sensor location.

One of the important factors in high-altitude guided (homing) flight is the coupling of body motion (angle of attack) into apparent inertial line-of-sight through variable boresight errors. A nose-mounted, hemispherical window, while having small flow-induced, look-angle-dependent boresight errors, has no angle-of-attack coupling, since the flow moves with body angle changes. All other forms of boresight error (including those from non-hemispherical windows, from dome expansion, or from side-mounted windows behind a nose shock) have boresight error slopes that couple angle-of-attack motion into apparent line-of-sight rate. Since side-mounted sensors experience the largest flow-induced boresight error, an estimate of coupling was made using the change in boresight error of central rays as a function of body angle of attack. This coupling was found to be very small, on the

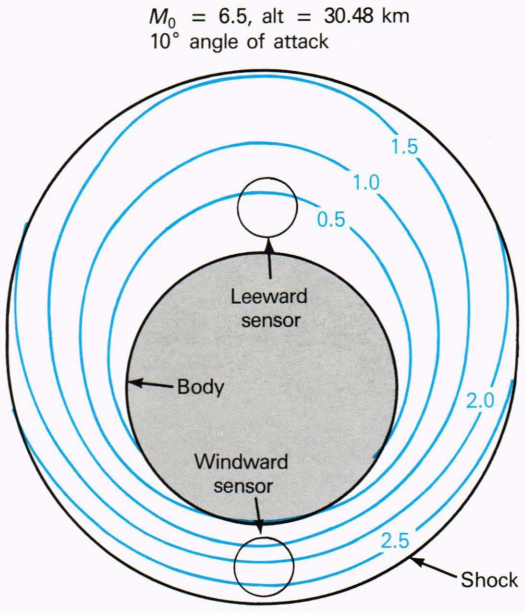

Figure 12—Crossflow density contours showing the effect of angle of attack on the flow field surrounding side-mounted optical sensors.

order of 0.0014 mrad per degree angle of attack for Mach 6 flight at sea level (and falling with altitude as a function of atmospheric density).

Aero-Optical Testing

The optical effects of shock wave impingement are difficult to predict. Preliminary experiments have been con-

ducted at the Propulsion Research Laboratory to measure optical effects of shock wave impingement on a hemispherical window. A fixed-angle optical system observes a collimated target with an optical system and linear detector array. This target is projected into the test system (located behind a hemispherical window at 45° from the flow direction). Once the test model is inserted into the hypersonic flow and the target signal is detected, a shock generator probe is lowered to sweep a shock across the hemispherical window, simulating the passage of a vehicle nose shock across a side-mounted window during a maneuver. Figure 5 shows shadowgraphs of the shock. A diagram of the test setup and a photograph of the optical test hardware are shown in Fig. 13.

A typical aero-optical test result is shown in Fig. 14. At time zero, the model is inserted into the hypersonic flow stream. As the model reaches its final position in the stream, a linear array of detectors begins to measure the signal from a collimated infrared target projected into the test cabin. The detector field of view is 0.5 mrad and the center-to-center spacing is 1 mrad. Changes in signal strength or distribution across the array indicate optical perturbations (in this case caused by shock interaction; see Fig. 5). Outputs from the four principal receiving detectors (channels 3 through 6) are shown in the lower portion of Fig. 14. The top portion shows the image centroid as calculated from the detector output for both pre-test (no flow) and test conditions. A transient perturbation is seen on all detector channels as the model reaches position. The pre-test measurement clearly shows a ringing (vibration) as the model is brought to rest. The ringing is masked by noise during the test that is likely caused by interaction of the hypersonic jet with still air in the test cabin or perhaps by vibration from the force of the flow. After the transients of inserting the model diminish, the shock-generating wedge is lowered and the shock–shock interaction traverses the window of the test system. The time of the shock interaction is marked on Fig. 14. No significant increase in angle noise or centroid shift was noted in this particular case, although a few possible (minor) effects are noted by arrows on Fig. 14. Further work is under way to improve the accuracy of these measurements in preparation for a comprehensive optical test program.

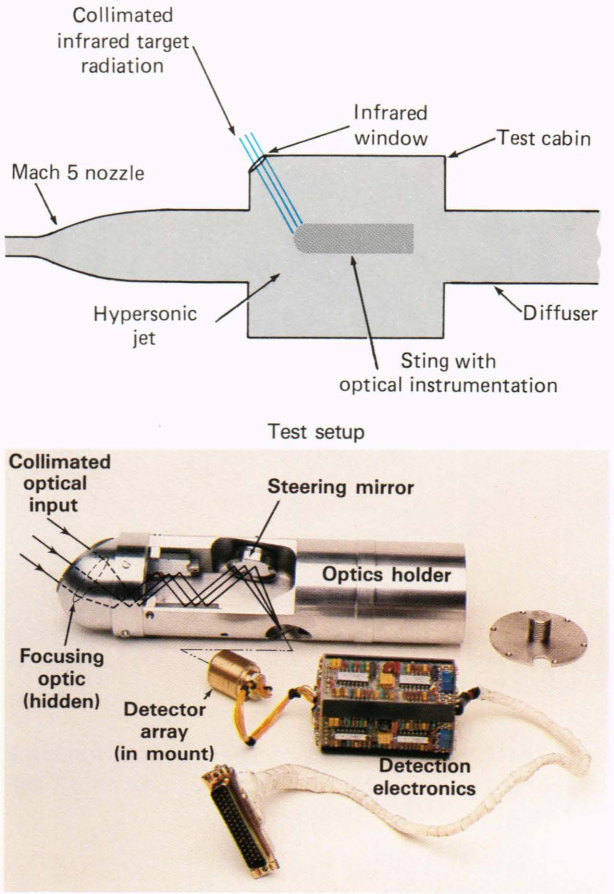

Figure 13—Sensor used to measure optical effects of hypersonic flow.

ACTIVE COOLING OF OPTICAL WINDOWS

As flight speeds increase and the thermal environment becomes severe, active thermal protection of windows becomes necessary. The optical performance of the window is degraded by changes in optical power caused by thermal expansion and refractive index change, the optical transmission is reduced by increased absorption, and the sensor performance is degraded by higher radiation levels. The structural integrity of the window may be in jeopardy in severe thermal environments. These problems associated with the thermal environment can be

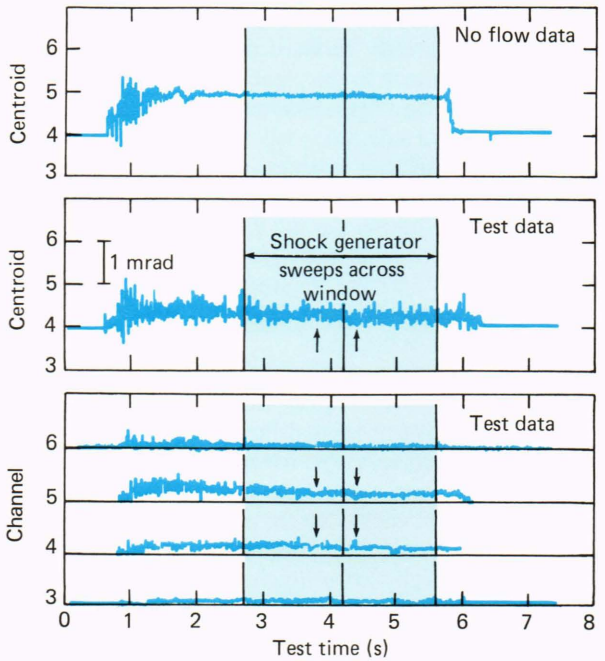

Figure 14—Measurement of optical spot's position during shock interaction in hypersonic flow. The upper portion shows the measured target centroid in (a) no-flow and (b) hypersonic flow conditions. The lower portion (c) shows the output of the individual detector channels during flow. Arrows mark possible shock interaction optical effects.

mitigated by maintaining the window material at acceptable temperatures with active, tangential slot cooling. On the other hand, optical effects caused by injecting coolant into the boundary layer are greater than those of the uncooled boundary layer.

Tangential Slot Cooling on Flat Plates

Tangential slot cooling injects a coolant gas along the window surface and parallel to the external stream. A schematic of the process is shown in Fig. 15. The window temperature is maintained at the coolant gas temperature as long as the mixing layer does not reach the window surface. When the mixing layer attaches to the surface, the surface will heat. Design of a satisfactory cooling system requires an accurate estimate of the coolant flow rate required to protect the window surface.

Determination of the cooling rate requirements of the tangential slot is based on a control volume approach. The conservation of energy (total enthalpy form) for steady-state, adiabatic wall conditions is

$$\dot{m}_{bl} H_{aw} = \dot{m}_c H_c + \dot{m}_{en} H_e \ , \qquad (7)$$

where the boundary layer energy ($\dot{m}_{bl} H_{aw}$) is the sum of the coolant energy ($\dot{m}_c H_e$) and the energy entrained from the edge of the boundary layer ($\dot{m}_{en} H_e$). Here $\dot{m}$ represents the mass flow rate per unit width. Conservation of mass is given by

$$\dot{m}_{bl} = \dot{m}_c + \dot{m}_{en} \ . \qquad (8)$$

Solving for the entrained mass flow rate in Eq. 8 and substituting into Eq. 7 yields the following expression for the coolant effectiveness, E_c,

$$E_c = (H_e - H_{aw})/(H_e - H_c) = \dot{m}_c/\dot{m}_{bl} \ . \qquad (9)$$

Unity coolant effectiveness implies zero entrainment from the external boundary layer. In that case ($E_c = 1$), the coolant gas insulates the window from the hot external stream. Zero cooling effectiveness ($E_c = 0$) implies that the coolant does not protect the surface at all. This control volume approach is consistent with previous analyses.[8,9]

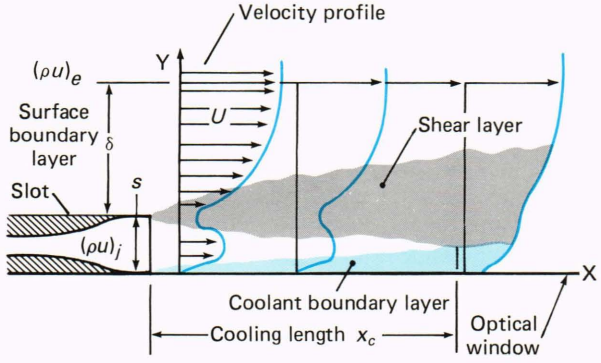

Figure 15—Sketch of tangential slot cooling along a window surface. This figure defines terms used to describe active surface cooling.

To predict the extent of the surface protected by the coolant gas, the coolant mass flow rate is given by

$$\dot{m}_c = (\rho u)_c \, s \ , \qquad (10)$$

and the boundary layer mass flow rate[7] by

$$\dot{m}_{bl} = 7/8(\rho u)_e \, \delta \ , \qquad (11)$$

where the boundary layer thickness, δ, is given by the incompressible-gas relationship

$$\delta/x = 0.37(Re)_x^{-1/5} \ , \qquad (12)$$

and where $(Re)_x$ is the Reynolds number, which is equal to $x(\rho u)_e/\mu_e$.

A dimensionless expression for the cooled surface length can be derived by substituting Eqs. 10 to 12 into Eq. 9 with $E_c = 1$. This approach assumes that the coolant gas and edge of the boundary layer have equal pressure. Performing the substitutions gives an expression for the ratio of the protected surface length to the slot height:

$$x_c/s = 4.1 \ m[(Re)_s \ \mu_c/\mu_e]^{0.25} \ , \qquad (13)$$

where x_c is the protected surface length; s is the slot height; m is the coolant-to-edge mass flux ratio, $(\rho u)_c/(\rho u)_e$; $(Re)_s$ is the slot Reynolds number, $(\rho u)_c s/\mu_c$; and $\mu_{c,e}$ is the absolute viscosity at coolant and edge conditions, respectively.

This control volume boundary layer approach breaks down for $m > 1.5$. Equation 13 allows one to estimate the coolant flow required for specified slot height, s; protected surface length, x_c; coolant temperature; and boundary layer edge conditions. Equation 13 then allows calculation of the coolant mass flux, and the coolant mass flow rate is determined from Eq. 10.

Tangential Slot Cooling of Inclined Surfaces and Blunt Bodies

Cooling of supersonic inclined surfaces is similar to the flat-plate analysis described above. An added benefit of mass injection over an inclined surface is the control of boundary-layer separation. The pressure rise associated with the inclined surface may be sufficient to cause the upstream boundary layer to separate, as shown in Fig. 16. The recirculating, separated flow region creates thermal and possibly optical problems. High heat transfer occurs where the shear layer attaches to the inclined surface. Mass (coolant) injection can reduce or eliminate the separated flow region.

A blunt optical window has high heating at the stagnation point. It may be necessary to cool that region to ensure survival and maintain acceptable optical performance. A similar control-volume boundary layer approach can be used to define the region of high cooling efficiency. This approach will differ from the flat-plate analysis because a different expression for the boundary-layer mass-flow rate is used. Little experimental data are available for the blunt-body case.

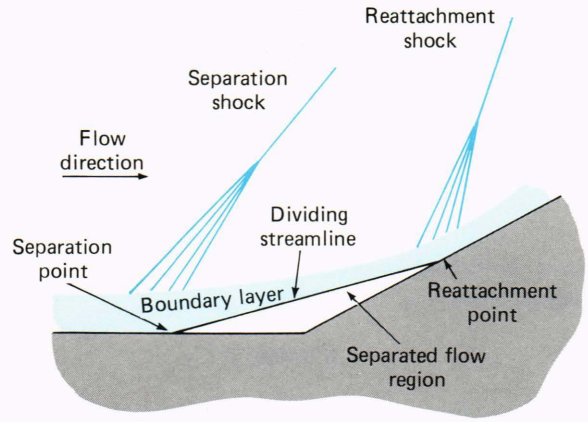

Figure 16—Boundary layer separation from a compression surface. Side-mounted windows may cause flow separation, which can be controlled by active cooling.

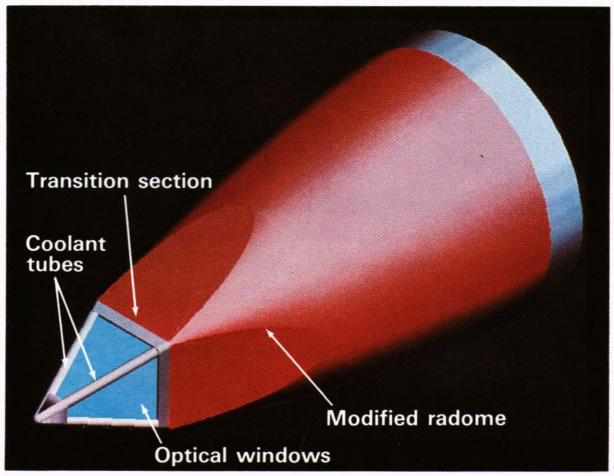

Figure 17—Window configuration for multiple-pane cooling being developed at APL.

Figure 17 shows a cooled window concept being developed under APL's Independent Research and Development program. This configuration, using several window panes, is also readily adapted to side-mounted sensors. Coolant passes along the top and side, if the windows are slotted. Gas exits the slots and separates the window from the high-temperature boundary layer, thus maintaining a cool surface. Slot dimensions were sized using a slightly modified form of Eq. 13. A test model is being constructed with testing of the cooling effectiveness and optical characteristics expected by the end of the year.

Optical Properties of Coolant Gases

Several gases have been proposed as fluids for film cooling of optical windows, including helium, argon, nitrogen, carbon dioxide, and sulfur hexafluoride. Transmission and refractive index measurements of the gases were made at high pressure (up to 6.9×10^6 Pa) and temperature (up to 775 K). The data were taken to determine the coolant gas with the best optical properties. In general, gases with low molecular weights are the most efficient coolants from a mass standpoint, while those with high molecular weights are volume efficient.

Table 2—Index of refraction parameters ($\lambda = 0.6328$ μm).

Gas	A ($cm^3/mole$)	B ($cm^6/mole^2$)	T^*
He	0.78	≃9	≃0
N_2	6.90	14	≃0
Ar	6.66	95	≃0
CO_2	10.2	1674	3.12
SF_6	17.5	1702	4.20

Note: The unit cm^3/mole is a reciprocal molar density.

Index of refraction measurements were made with a laser interferometer operating at 0.633 μm and a high-temperature, high-pressure gas cell. Measurements were made as a function of pressure and temperature and were fitted to an equation of the form

$$n - 1 = A(P/RT) + B(P/RT)^2 \times \exp[T^*(295/T - 1)] , \quad (14)$$

where the parameters A, B, and V are experimentally determined. Note that this equation is a higher order form of the Gladstone–Dale relationship of Eq. 1, with density in a number-per-unit-volume form (P/RT). The pressure-squared term in the refractive index is entirely attributable to nonideal gas behavior. Depending on the size of the virial coefficients and the strength of collision-induced absorption, the quadratic term may be important. Table 2 gives the index parameters for the gases. CO_2 and SF_6 have significant quadratic terms.

A Fourier-transform spectrometer and the same high-temperature, high-pressure gas cell were used to measure transmittance in the 1800 to 5000 cm^{-1} spectral range. Measurements were made of the significantly absorbing gases—nitrogen, carbon dioxide, and sulfur hexafluoride—as well as water vapor. Pressures to 6.9×10^6 Pa and temperatures to 690 K were used to determine the pressure- and temperature-dependence of transmission (and, therefore, emission).

Figure 18, an example of transmission measurements, shows pressure-dependent room-temperature spectra of carbon dioxide. The zero absorption level of each spectrum is offset in order of increasing pressure. Each absorption band is identified by number (1 to 11): bands 1, 2, 5, 8, 9, 10, and 11 are fundamental bands; 3 and 4 are hot bands; and 6 and 7 are collision-induced bands. The fundamental and collision-induced bands decrease in strength with temperature while the hot bands will grow. Carbon dioxide is an undesirable gas in the spectral region from 2000 to 2600 cm^{-1} because of high absorption and emission. It is also generally undesirable as a coolant because of its high index of refraction compared with air (image scintillation is caused by mixing of gases of different indexes).

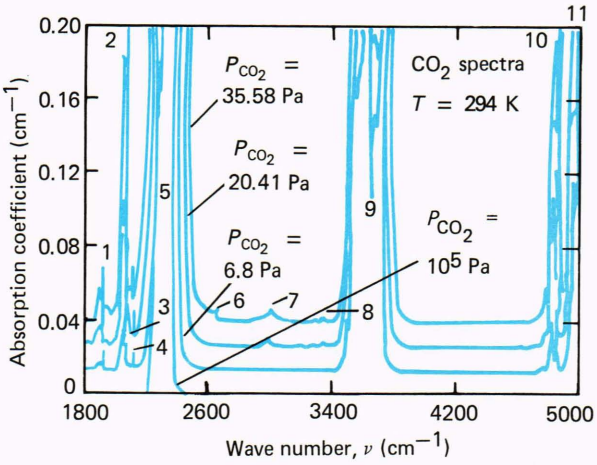

Figure 18—Carbon dioxide spectra at room temperature. Fundamental bands are labeled 1, 2, 5, 8–11; 3 and 4 are hot bands; and 6 and 7 are collision-induced bands. The high absorption of carbon dioxide makes it an undesirable coolant for optical windows of infrared sensors.

Argon and nitrogen are the most acceptable coolant gases from an optical standpoint. Absorption is negligible and the index of refraction closely matches that of air. Helium is also nonabsorbing but has a very low refractive index, while carbon dioxide and sulfur hexafluoride have high refractive indexes and absorb in many spectral regions.

Further measurements of water vapor and nitrogen are presented in the article by Thomas elsewhere in this issue.

WINDOW MATERIAL EFFECTS

The effects on image sensing through heated optical windows include distortion caused by thermal expansion and refractive index changes, greatly increased radiation from the window generated by high temperature, and transmission changes caused by increasing absorption with temperature. Thermal expansion and change in refractive index result in focus change (blur) and boresight shift, while radiation can contribute to heating of sensor components and significant loss of sensitivity. To quantify the effects of high temperature, it is necessary to determine window material properties over the temperature range of interest. Since most optical properties must be measured over both frequency and temperature, a large quantity of data is needed. The volume of experimental data is reduced if the properties can be accurately modeled.

Work on determining high-temperature optical properties of windows for high-speed flight has focused on three aspects: (a) developing techniques to measure sample properties such as transmittance, reflectance, scatter, and optical index, (b) developing material models to estimate properties in hard-to-measure regions, and (c) estimating the requirements for measurement (or prediction) accuracy needed to support sensor performance prediction. Measurements were made in APL's Infrared Laboratory and supplemented by published information. Our work has focused on various forms of four high-temperature ceramics: sapphire (aluminum oxide), spinel (aluminum magnesium oxide), ALON (aluminum oxynitride), and yttria (yttrium oxide) (see the boxed insert). These materials can be fabricated into transparent, low-scatter,

HYPERSONIC WINDOW MATERIALS

Materials considered for hypersonic optical windows are selected on the basis of high-temperature stability, thermal shock resistance, and good optical properties. Oxides and nitrides satisfy these criteria. The four measured materials—ALON, sapphire, spinel, and yttria—are commercially available in high-quality optical form. All are clear and colorless, although thicker samples of polycrystalline materials may appear slightly cloudy because of scatter. All have good infrared transmission to at least 4 μm.

ALON is a hard, polycrystalline, reaction-sintered material made by Raytheon. It is a cubic aluminum oxynitride spinel, with the approximate composition of $9Al_2O_3$-5A1N. The material has high strength and low scatter and can be manufactured as flat plates or domes in sizes up to 12.7 cm in diameter.

Sapphire is an extremely strong and hard hexagonal single crystal (Al_2O_3) made by many companies. Crystals are grown from the melt and have very low scatter. As a hexagonal crystal, sapphire is anisotropic and exhibits birefringence. APL samples are HEMLITE-grade provided by Crystal Systems, Inc., oriented in the (0001) direction. Windows 20.3 cm long can be made.

Spinel is a hard, moderately strong, cubic polycrystalline material ($MgAlO_4$) that can be made into windows and domes up to 12.7 cm in diameter by several methods including hot-pressing, hot isostatic pressing, and flame fusion. Samples were provided to APL by Coors Porcelain and Raytheon.

Yttria is a moderately hard, moderately strong cubic polycrystalline material (Y_2O_3) being developed as a window material. Raytheon produces a pure yttria, while GTE Laboratories has developed a toughened yttria by adding approximately 9% lanthana (La_2O_3). The latter form is harder, stronger, and has greater fracture toughness at the expense of lower thermal conductivity. Both forms were investigated and found to have similar optical properties.

Several other materials have been proposed for hypersonic windows, including magnesium oxide (MgO), cubic zirconia (ZrO), aluminum nitride (AlN), and some of the mixed oxides. None of these materials is as well developed as those described above.

Effective and practical cooling systems will allow use of materials with reduced thermal shock resistance and, if continuous cooling can be achieved, lower temperature (e.g., longer wavelength materials).

high-strength windows capable of withstanding both high temperatures and extreme thermal stress of the rapid aerodynamic heating of hypersonic flight.

Window Optical Property Measurements

The most significant optical property of a window at high temperature is its emission. Since the window cannot be thermally insulated by conventional techniques, the total window radiation governs the heat transfer into the interior of the sensor and affects the ultimate window temperature via radiant heat transfer. For high-sensitivity infrared sensors, the amount of window radiation within the sensor spectral bandpass governs system noise and possibly dynamic range. Temperature also changes the optical thickness of windows both by expansion and by index change. As noted above, the nonuniform thermal expansion of hemispherical windows significantly affected optical resolution. Changes in optical index are expected to have an effect of similar magnitude.

Optical materials considered for hypersonic windows are transparent from the ultraviolet through the near-infrared. Table 3 summarizes properties of typical window materials. The short-wavelength absorption is caused by electronic transitions and the infrared absorption cutoff results from lattice vibrations and their high harmonics (called multiphonon processes). These optical materials have a fundamental lattice frequency, ω_0, in the far infrared and are typically transparent above $3\omega_0$. The multiphonon absorption edge shifts to higher frequencies with increasing temperature. It is therefore necessary to characterize the material absorption (and, therefore, emission) as a function of temperature.

Transmission spectra of two different sample thicknesses are measured at room temperature using a Fourier-transform spectrometer. The ratio of transmittances (τ_2/τ_1) and difference in thickness $(t_2 - t_1)$ of the samples are used to eliminate surface effects and estimate room temperature absorption coefficient, α:

$$\alpha = -\ln (\tau_2/\tau_1)/(t_2 - t_1) \; . \qquad (15)$$

The absorption coefficient at elevated temperature is determined by comparing the heated-sample spectrum to a room-temperature spectrum to determine temperature-dependent change in absorption. Experimental methods have been developed to maintain good spectrometer source stability and to reduce the time between sample measurements, thus improving experimental accuracy. The required absorption accuracy needed to predict sensor performance is typically 20%. Figure 19 shows typical measurements and model results (discussed below). These values can be used to estimate the normal emissivity, ϵ_λ, in terms of the thickness and single-surface reflectivity, r:

$$\epsilon_\lambda = (1 - r)(1 - e^{-\alpha t}) \; . \qquad (16)$$

The normal-incidence, single-surface reflectivity is approximated by $(n - 1)^2/(n + 1)^2$. Further absorption data, including single-frequency laser measurements, are reported in Ref. 10.

The temperature-dependent refractive index (n) has been measured using an automated fringe-counting la-

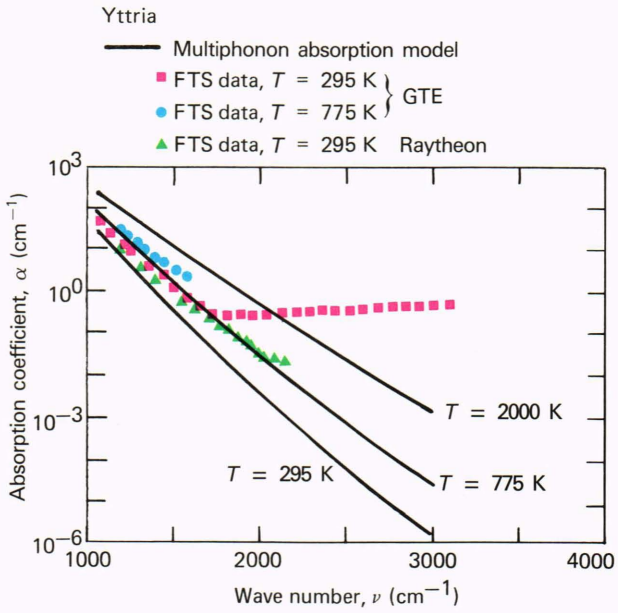

Figure 19—Extinction measurements and multiphonon model predictions for yttria. Measurements via Fourier-transform spectrometry (symbols) and model predictions from the multiphonon model (lines) show good agreement at smaller wave numbers. The model can be used to predict absorption at high temperature or in regions masked by scatter.

Table 3—Optical properties of durable, high-temperature ceramics.

	*Index of Refraction,**		*Melting*	*Room Temperature*
Material	*n*	*dn/dT* (K^{-1})	*Temperature* (*K*)	*Transparent Region*** (cm^{-1})
ALON	1.79	7.5×10^{-6}	2415	2100 - (40,000)?
Sapphire	1.765	6.1×10^{-6}	2315	2000 - 55,000
Spinel	1.715	7.4×10^{-6}	2410	1875 - 50,000
Yttria	1.925	-1.6×10^{-6}	2695	1400 - (50,000)?

*Index of refraction at 0.6328 μm
**Room-temperature absorption coefficient exceeds 1 cm^{-1}

ser interferometer operating at 0.6328 μm. The sample is placed in one leg of the interferometer and heated in a vacuum cell. Once the sample temperature reaches equilibrium, the change in optical path length can be determined to one-quarter wavelength. Refractive index change can then be determined if the thermal expansion coefficient is known. Values of the derivative of index with temperature (dn/dT) derived from these measurements are given in Table 3.

Reflection measurements in the spectral region of the fundamental (one-phonon) lattice vibrations are made to deduce optical constants for estimating total hemispherical absorption (emission). These data are used in a model to determine the complex refractive index, as described below.

Modeling Properties of Optical Windows

Several models have been developed to aid in determining optical properties to extend measurements beyond the measured region. The principal models are a quantum-mechanical multiphonon model and a classical single-phonon model.

The multiphonon model[10] determines the absorption coefficient from spectral measurements made at two or more temperatures. The model uses a Morse potential that leads to an exact solution to the Schrödinger equation. The phonon distribution function is determined by an asymptotic solution of the central-limit theorem. Statistical parameters of the phonon distribution function are determined from sapphire data. Those parameters are then scaled to each material by its maximum longitudinal optical-mode frequency, as determined from the reflectance spectrum. Dissociation energy and scaling parameters are determined from transmission measurements. The model represents the absorption coefficient as a function of frequency and temperature and can be used to interpolate and extrapolate the intrinsic absorption coefficient to nonmeasured conditions of interest. Of particular importance is the determination of absorption beyond the 775 K temperature limit of our measurements and extrapolation of the intrinsic absorption edge to high wave numbers, where measured extinction is dominated by scatter (i.e., in spectral regions where absorption is obscured by scatter). Figure 19 shows the model results that extend measurements to both higher temperature and lower absorption (higher wave number) conditions.

Optical index data are determined from a classical model of the fundamental lattice vibrations. The method is a simpler alternative to a Kramers–Kronig analysis. Reflection measurements are made at near-normal incidence and differentiated to determine the frequency location of the principal lattice vibrations, called optical modes.[11] Once the locations of the vibrational modes (ν_n) are known, the widths (δ_n) and strengths ($\Delta\epsilon_n$) of the modes are determined using a classical representation of the dielectric constant ϵ:

$$\epsilon(\nu) = \epsilon_\infty + \sum_n \frac{\Delta\epsilon_n \, \nu_n^2}{\nu^2 - \nu_n^2 + i\delta_n \nu} \qquad (17)$$

and

$$\epsilon_0 = \epsilon_\infty + \sum_n \Delta\epsilon_n \, , \qquad (18)$$

where ϵ_0 and ϵ_∞ are the dielectric constants at low and optical frequencies, respectively. Combining the determined transverse (ν_n) and longitudinal optical modes (Eq.18), the Lyddane–Sachs–Teller relationship[12] and reflectance data parameters of Eq. 16 can be determined. The complex refractive index is the square root of the complex dielectric constant. Results from sapphire were compared with published model parameters to evaluate the method. The model was then applied to ALON, spinel, and yttria. Figure 20 shows the ALON room-temperature refractive index derived using this method. Optical index data can be used to estimate total hemispherical and total direction emissivity of optical windows for radiative transfer estimates.

SUMMARY AND CONCLUSIONS

The high pressure, temperature, and radiation of hypersonic flow and heat transfer to sensor windows alter the performance of a sensor experiencing this environ-

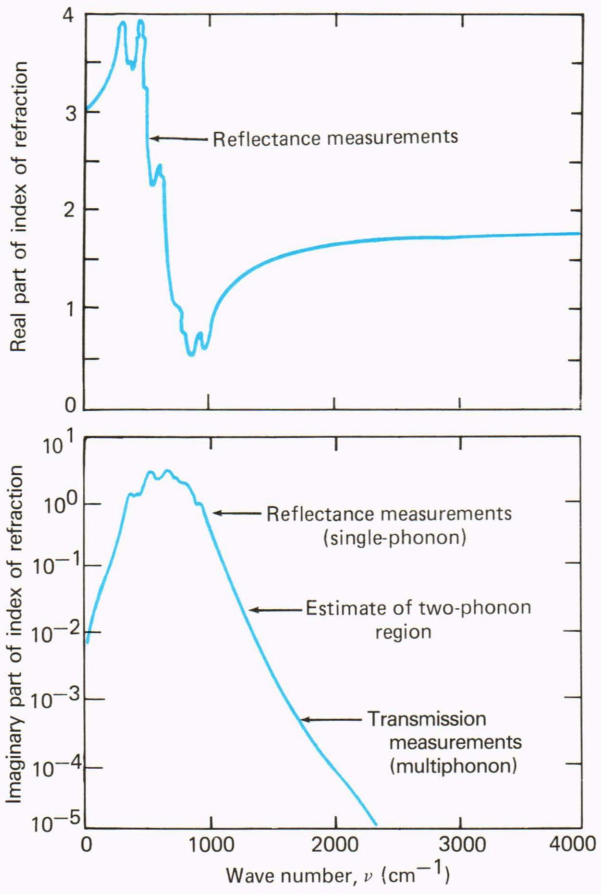

Figure 20—Room-temperature optical constants of ALON (aluminum oxynitride) derived from transmission and reflectance measurements. The optical constants are used to characterize the material properties.

ment. Sharp density gradients, shock interactions, turbulence, and coolant mixing alter the resolution, focus, and boresight of optical sensors. Although these flow effects are small, they can significantly affect the performance of moderate- to high-resolution sensors and couple vehicle body motion into position measurements or tracking systems.

We have shown that flow calculations can be coupled with ray-trace programs to estimate optical aberrations and boresight shifts in hypersonic flow. For simple cases (e.g., axisymmetric flows), optical effects are small but significant compared with optical resolution in the visible. More complicated flow conditions, such as shock–shock interaction, must be examined experimentally. We have demonstrated the capability of making optical performance measurements in hypersonic flow.

Elevated-temperature gas surrounding optical windows in hypersonic flight creates high aerodynamic convective heat transfer and contributes significant infrared radiation into the sensor. The rapidly heating window distorts, changes refractive index, and begins to emit radiation. Geometric and refractive-index changes in the window typically cause optical distortions greater than those of the hypersonic flow alone. Radiation from the flow gas and the heated window contribute significant radiative heat transfer to interior sensor components and greatly raise the background radiance seen by infrared sensors.

Measurements of gas absorption allow us to quantify emission from high-temperature and high-pressure gases surrounding a sensor window, as well as the radiation and transmission loss caused by coolant gases. We have established the use of heat transfer and strain calculations to determine optical distortion caused by window thermal expansion. Both measurements and models of window material emissivity are now available to characterize intrinsic emission as a function of wavelength and temperature.

As flight speed increases, active cooling of windows (and perhaps of other surfaces) will be needed to operate sensors. We have developed methods of designing film cooling systems and predicting performance. We have also made optical measurements of coolant gas properties needed to determine sensor performance with various coolants. We are currently developing a test model to measure cooling effectiveness and optical performance in hypersonic flow.

Work quantifying the optical effects of hypersonic flight has concentrated on developing fundamental calculation and measurement methods. As data or material properties are accumulated, calculation capabilities verified, and measurement methods proven, this expertise will be applied to development and test of sensors for hypersonic vehicles. These activities are expected to continue for several years.

This work was supported by APL Independent Research and Development funding as part of the Infrared Sensor Technology Project. Other tasks of this project will be reported in the future.

REFERENCES

[1] G. J. Zissis and W. L. Wolfe, *The Infrared Handbook*, Office of Naval Research, Washington, D.C., 24-16 (1978).
[2] F. M. White, *Viscous Fluid Flow*, McGraw-Hill, New York, pp. 627–629 (1974).
[3] F. S. Billig, "Shock Wave Shapes around Spherical and Cylindrical-Nosed Bodies," *J. Spacecr. Rockets* **4**, 822–823 (1967).
[4] B. E. Edney, "Effect of Shock Impingement on the Heat Transfer around Blunt Bodies," *AIAA J.* **6**, 15–21 (1968).
[5] F. D. Hains and J. W. Keyes, "Shock Interference Heating in Hypersonic Flows," *AIAA J.* **10**, 1441–1447 (1972).
[6] A. R. Wieting and M. S. Holden, "Experimental Study of Shock Wave Interference Heating on a Cylindrical Leading Edge at Mach 6 and 8," AIAA 22nd Thermophysics Conf., Paper 87-1511, Honolulu (1987).
[7] R. W. Bruns, J. H. Panesci, W. J. Tropf, and L. B. Weckesser, *Independent Research and Development: Infrared Sensor Technology Program Test Plan*, JHU/APL TG 1349 (1985).
[8] J. L. Stollery and A. A. M. El-Ehwany, "A Note on the Use of a Boundary Layer Model for Correlating Film-Cooling Data," *Int. J. Heat & Mass Transfer* **8**, 55–65 (1965).
[9] L. W. Carlson and E. Talmor, "Gaseous Film Cooling at Various Degrees of Hot Gas Acceleration and Turbulence Levels," in *Heat and Mass Transfer in Boundary Layers*, Vol. 1, N. Afgan, Z. Zaric, and P. Anastasijevic, eds., Pergamon Press, New York, pp. 177–198 (1973).
[10] M. E. Thomas, R. I. Joseph, and W. J. Tropf, "Infrared Transmission Properties of Sapphire, Spinel, and Yttria as a Function of Temperature," in *SPIE Vol. 683: Infrared and Optical Transmitting Materials*, SPIE, Bellingham, Wash., pp. 41–48 (1986); also see "Infrared Transmission Properties of Sapphire, Spinel, Yttria, and ALON as a Function of Temperature and Frequency" (to be published in *Appl. Opt.* **27** (1988)).
[11] R. I. Joseph and M. E. Thomas, "Differential Reflectance Spectroscopy: A Direct Determination of Long Wavelength Optical Mode Frequencies in Polar Crystals," *Physica Status Solida* (*b*) **141**, K163–K166 (1987).
[12] R. H. Lyddane, R. G. Sachs, and E. Teller, "On the Polar Vibrations of Alkali Halides," *Phys. Rev.* **59**, 673–676 (1941).

THE AUTHORS

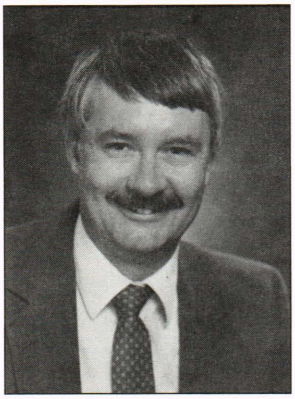

WILLIAM J. TROPF was born in Chicago in 1947. He received a B.S. degree from the College of William and Mary (1968) and a Ph.D. degree from the University of Virginia (1973), both in physics. He is now the supervisor of the Electro-Optical Systems Group in APL's Fleet Systems Department. Dr. Tropf has been engaged in the development and testing of advanced missile guidance systems since joining APL in 1977. His activities have encompassed both radar and infrared sensors, including atmospheric, target, and background modeling; signal processing for clutter suppression; and material properties. He has worked on hypersonic optical sensor development and test since 1981.

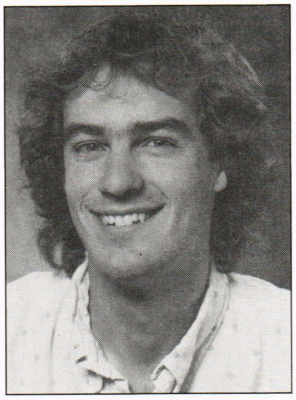

TERRY J. HARRIS graduated in 1982 from the University of Colorado with a B.S. degree in engineering physics. He is a member of the Electro-Optical Systems Group, where where he specializes in geometric optics, lens and optical system design, and ray-trace analysis. He is a member of the Society of Photo-Optical Instrumentation Engineers. Mr. Harris has designed optical systems for ground and space instruments, as well as the optics for target projection systems and optical measurements in hypersonic flow. He also conducted the aero-optical analysis reported in the article in this issue. He is now designing the optical system for a solar vector magnetograph instrument.

MICHAEL E. THOMAS's biography can be found on p. 369.

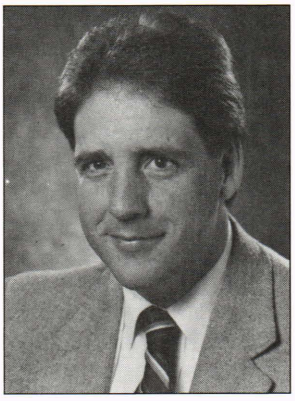

STEVEN A. LUTZ was born in 1953 in Harrisburg, Pa. He attended West Virginia University, receiving a Ph.D. degree in mechanical and aerospace engineering in 1984. His dissertation research dealt with the sampling efficiency of gas–solid aspiration probes for highly turbulent flow streams. While at West Virginia, he taught undergraduate thermodynamics. Dr. Lutz worked from 1983 to 1985 for the Department of Energy, where he analyzed and designed optical access ports for laser diagnostic instrumentation of coal conversion systems. Since 1985, he has been a member of APL's Aeronautics Department. His interests include aerodynamic heating, supersonic and hypersonic turbulent boundary layer flows, and nonintrusive instrumentation for high-speed testing.